Journal of Wood Science

ORIGINAL ARTICLE

Open Access

Investigation of mechanical properties and elucidation of factors affecting wood-based structural panels under embedment stress with a circular dowel II: detailed observation for plywood and OSB using DIC and CT scanning

Ryutaro Sudo[1*] and Kenji Aoki[2]

Abstract

Although embedment properties are vital to timber engineering, the behavior and strain distributions in wood-based panels have not been clarified in detail. Our early studies suggested four possible causes of failure behavior and strain distribution: (i) two types of failure behavior (in-plane and out-of-plane failure); (ii) enlargement of the stress-spreading range with increasing load step; (iii) reduction of the stress-spreading range (normalized by dowel diameter) with increasing dowel diameter; and (iv) preferential stress spreading in the vertical and horizontal directions along the strong and weak-axis specifications, respectively. However, these hypotheses were not supported by actual observations. The present study aims to observe and clarify the surface strain distribution via digital image correlation and the internal failure behavior via computed tomography scanning. Most results of the wood-based panel specimens (plywood and oriented strand board) did not contradict the above hypotheses. The failure behaviors of plywood and oriented strand board are likely determined by the direction of the veneer fibers and the layer's position, respectively. Within the strong axial layer of plywood, fibers on both sides of the dowel were densified by fibers dissociated immediately above the dowel, whereas the weak axial layer in plywood was deformed like a timber under partial compression perpendicular to the grain. In contrast, oriented strand board under an embedding stress exhibited a circularly distributed strain and a dispersed void area in its outer layer. Densification was observed only in the inner layer.

Keywords Wood-based structural panel, Plywood (PW), Oriented strand board (OSB), Digital image correlation (DIC), Computed tomography scanning (CT scan), Embedment, Bearing, Multi-modal approach

*Correspondence:
Ryutaro Sudo
sudoryutaro0513@ffpri.affrc.go.jp
[1] Forestry and Forest Products Research Institute, Matsunosato, Tsukuba, Ibaraki 305-8687, Japan
[2] Department of Biomaterials Sciences, Graduate School of Agricultural and Life Sciences, The University of Tokyo, 1-1-1 Yayoi, Bunkyo-Ku, Tokyo, Japan

Introduction

The mechanical properties of timber under the stress generated by hard cylindrical dowels (e.g., nails and bolts), herein defined as the "embedment properties", strongly affect the performance of the connections in timber constructions. The embedment properties of timber have been extensively investigated. Various studies have gathered experimental data while varying the comprehensive parameters (e.g., dowel diameter, pilot hole, edge distance, and end distance), arranged the failure modes, clarified the process of fracture and stress spreading, and suggested mechanical models based on experimental results. In contrast, the embedding properties of wood-based panels are seldom studied and the failure behavior and influence of various parameters on wood-based panels remain unclear.

Previously, we investigated the effects of different parameters on the embedment properties (failure behavior, ductility, yield stress, and maximum stress) of wood-based panels (plywood (PW), oriented strand board (OSB), particleboard, medium-density fiberboard, and hardboard) [1]. The observed trends suggested four possible causes of failure behavior and stress spreading (see Fig. 1): (i) when the edge distance is sufficient, both in-plane failure and out-of-plane failure can occur; (ii) the stress-spreading range is larger under maximum stress than under the yield stress; (iii) the stress-spreading range (normalized by the dowel diameter) reduces with increasing dowel diameter; and (iv) the stress generated by the embedment pressure preferentially spreads vertically and horizontally along the strong and weak-axis specifications, respectively. Here, the strong and weak-axis specifications denote that the fibers in the surface layers are oriented parallel and perpendicular to the load direction, respectively.

The present study attempts to verify these hypotheses through detailed observations involving digital image correlation (DIC) and computed tomography (CT) scanning.

DIC measures the surface stress distribution by tracing the movements of random dot patterns. In recent years, DIC has revealed various deformation behaviors of timber, such as radial compression behavior [2], elastoplastic surface displacement of partially compressed wood [3], the strain distribution adjacent to the loading plate [4], and the strain in a traditional half-lapped joint [5]. DIC has also been employed in studies on dowel connections [6, 7] and the embedment properties of timber [8–11].

Meanwhile, CT scanning has observed the internal behavior of wood; in particular, its moisture content, anatomical structure, and decay [12–14]. Some studies have applied CT scanning to timber engineering. Based on simultaneous loading tests and CT scanning, researchers have reconstructed the three-dimensional (3D) microscale deformations of wood during uniaxial compression [15] and bending [16]. The bending deformation of bolts in connections has also been observed in CT scans [17]. From the CT-scanned density profile immediately around a screw, the authors of [18] precisely regressed the withdrawal strength of the screw against the density of cross-laminated timber.

Some studies adopted a multimodal approach combining DIC and CT scanning [19, 20]. For example, Leader et al. [20] carried out an embedment test with 12-mm steel dowels and timber under three loading cycles: (i) the end point of the specimen adjustment during loading (~ 1.5 kN), (ii) the quasi-elastic limit, and (iii) the maximum dowel displacement. The samples were subjected to DIC and CT scanning during loading and after each loading step, respectively.

Elucidating the stress distribution and failure process of wood-based panels under embedding stress is important for formulating theoretical and mechanical models of embedding performance. However, the failure behavior of wood-based panels under an embedding stress has not been previously reported.

The visualized results of multimodal approaches provide an intuitive understanding of failure behavior. Therefore, the present study adopts the method proposed by Leader et al. [20]. In fact, CT scanning more effectively observes the failure behavior of wood-based panels than timber. As CT scanning is limited to the measurable volume, it is more suitable for lower-volume wood-based panels than for large-volume timber. To overcome the volume limitation, the authors of [20] isolated the core cylinder just around the dowel for observation via CT scanning, which shortened the practical end and edge distances and supposedly affected the result. In addition, wood-based panels are layered structures with different properties in their outer and inner parts. Therefore, observing the behavior of the inner layer via CT scanning is more important in wood-based panels than in timber samples.

The present study investigates the failure behavior of wood-based panels via the multimodal approach to assist the construction of a theoretical model. In addition, we verified whether the results of the multimodal approach support our earlier hypotheses [1]. To simplify the discussion, we limit our analysis to PW and OSB panels. These panels were selected because they share the same in-plane orthotropy and long history of structural use.

Materials and methods

Specimens

Table 1 gives the fundamental properties of the specimens (PW and OSB panels), including their densities, moisture contents, tensile strengths, internal bond strengths, in-plane shear strengths, and information regarding their standard classifications. The embedment test was conducted along the strong and weak axes, meaning that the load was applied parallel and perpendicular to the fibers on the surface layer, respectively. To denote specimens tested along their strong or weak axes, we append "-s" or "-w" to the specimen name. For

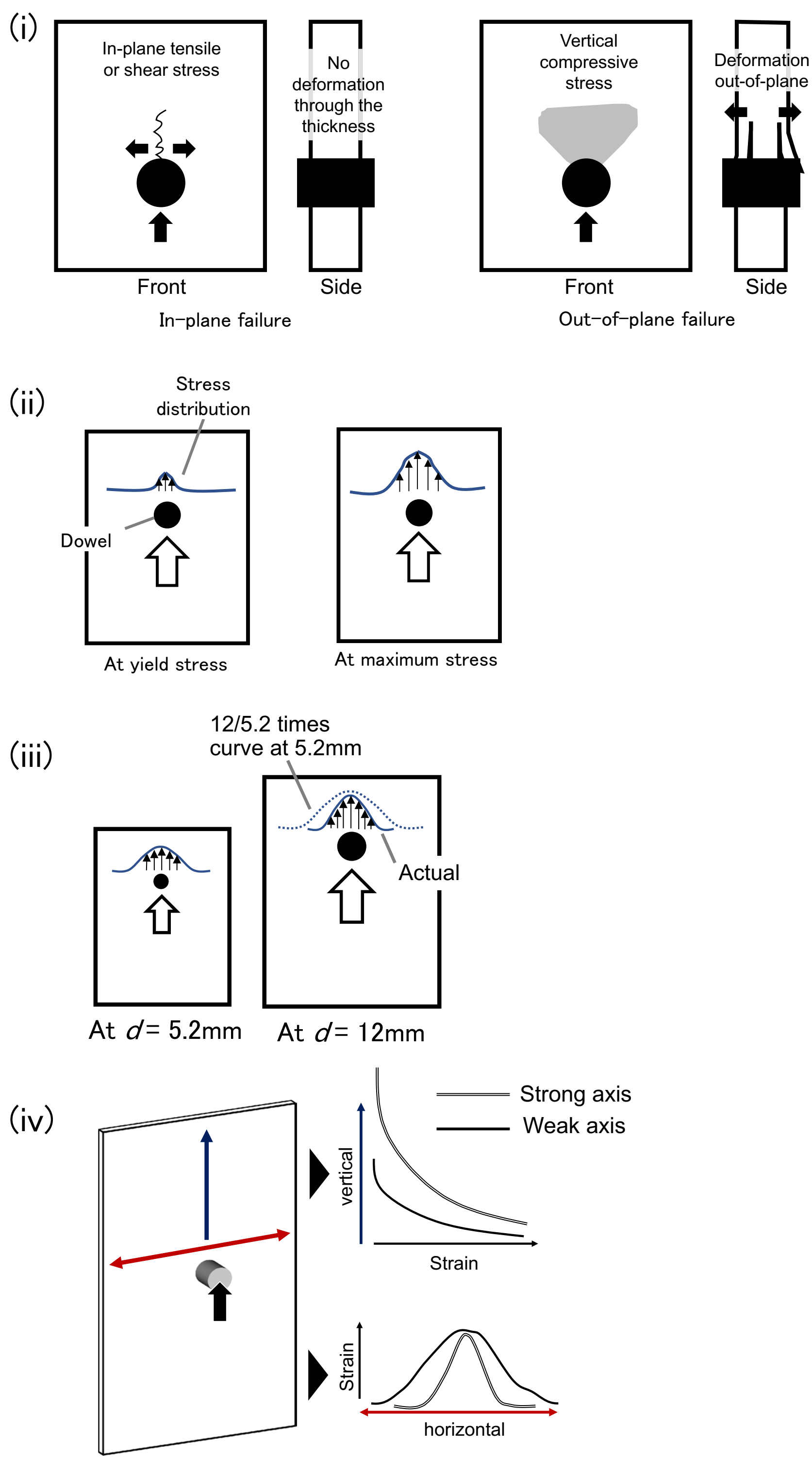

Fig. 1 The four hypotheses proposed in our earlier study [1]. Hypothesis (**i**) proposes that when the edge distance is sufficient, both in-plane failure and out-of-plane failure can occur. Hypothesis (**ii**) proposes that the stress-spreading range is larger under maximum stress than under the yield stress. Hypothesis (**iii**) proposes that the stress-spreading range (normalized by the dowel diameter) reduces with increasing dowel diameter. Hypothesis (**iv**) proposes that the stress generated by the embedment pressure preferentially spreads vertically and horizontally along the strong and weak-axis specifications, respectively

Table 1 Fundamental properties of the plywood (PW) and oriented strand board (OSB) panels

		Density (kg/m^3)	MC (%)	In-plane tensile properties		Internal bond properties		In-plane shear properties		Other information
				Strength (MPa)	Elastic modulus (GPa)	Strength (MPa)	Elastic modulus (GPa)	Strength (MPa)	Elastic modulus (GPa)	
PW	Ave	421	8.5	16.3	6.85	1.585	0.0280	5.55	0.674	Wood species; Cryptomeria japonica (Japanese cedar) Number of layers; 5, class; 2nd, use; for structural use [21]
	S. D	10	1.7	4.1	0.96	0.147	0.0045	0.46	0.065	
OSB	Ave	651	6.6	18.7	6.51	0.724	0.0181	11.30	2.063	Number of layers; 3, class; 4th [22]
	S. D	41	0.2	3.1	1.05	0.121	0.0039	1.15	0.305	

Ave. (average) and S.D. (standard deviation) of three mechanical tests according to ASTM D 1037 [23]

example, PW-s indicates the strong axis, whereas PW-w indicates the weak-axis. All panels were 9 mm thick. The dowels were of two diameters (d=5.2 mm or 12 mm) and identical in type to those of our earlier study [1]. The edge and end distances were 7d. A pilot hole equal to d was formed before the test. For each of the eight specifications targeted in this study, we prepared and tested two specimens.

Testing procedure

Figure 2 is a schematic of the testing procedure. The force was applied and removed during each of three loading steps. DIC was conducted during the loading process and CT scanning was conducted after unloading the force. The loading test apparatus was similar to that in the earlier study (Fig. 3). A monotonic tensile force was applied at 0.5 mm/min (d=5.2 mm) and 1 mm/min (d=12 mm) in the first and second loading cycles. The test speed was doubled in the third cycle. The load and displacement were measured as described in our earlier study [1].

The loading steps were determined as follows. Based on the results of our earlier study (see Table 2), the load in step 1 was one-half the maximum load. In step 2, the point was at which load lowered by 0.1 kN, which can be regarded as the point at the maximum load. In step 3, the point was d from the displacement at 0.1 kN in the loading process.

For DIC measurements of the strain distributions on the specimen surfaces, black dots on a white surface were randomly painted on the faces of the specimens. The surfaces were imaged by a digital SLR camera (canon EOS Kiss X90 EF-S18-55 mm IS II lens kits) at 0.2 Hz during the loading process. To ensure constant surface illuminance, the specimens were illuminated by a ring light in the darkroom during the DIC procedure. A resolution of the images was 6000×4000 pixels. The images were analyzed using DIC software, the GOM Correlate software package, and GOM Gmbh (Braunschweig, Germany) [24]. The GOM software measures local strains from deformation images using an automated computer algorithm, as shown in Fig. 4. The correlation parameters for the evaluation were facet size of 19 pixels and grid spacing of 16 pixels.

Figure 5 shows the specimen in the CT scanning apparatus (v|tome|x L300, Baker Hughes, Japan, Tokyo). To improve the efficiency of testing, several specimens were sandwiched between foam core boards and tested at the same time. The specimens were scanned at a 200 kV and 200 μA source output level with no filters. The scanning distances to the detector and specimens were 1400 and 962.5 mm, respectively. The number of angular projections (0.18°) was 2000 with 0.75 s of exposure time per projection. The CT images were analyzed using MyVGL (volume graphics, Heidelberg, Germany) [25]. The resulting 3D and cross-sectional images are shown in Fig. 6. The 3D reconstruction volumes were composed of grayscale voxels with dimensions of (275×275×275) μm^3. As the brightness of the pixels corresponds to their density, the internal deformation behavior can be inferred from these images.

Additionally, we could not observe visible fracture in mechanical behavior in this study since the displacement was limited to 1d and it was too small to become fractured completely. Therefore, we judged the fracture only based on the images of DIC and CT scanning.

DIC results

Analysis method

Regarding the load direction as the y-axis, the x-, y- and shear–strain distributions were obtained along five lines (see Fig. 7). As shown in representative strain distributions (Fig. 8), the strain was stronger near the dowel than in other areas and could not be measured in some areas due to failure. The failed areas were considered as areas of local strain and fracture spread caused by embedding stress.

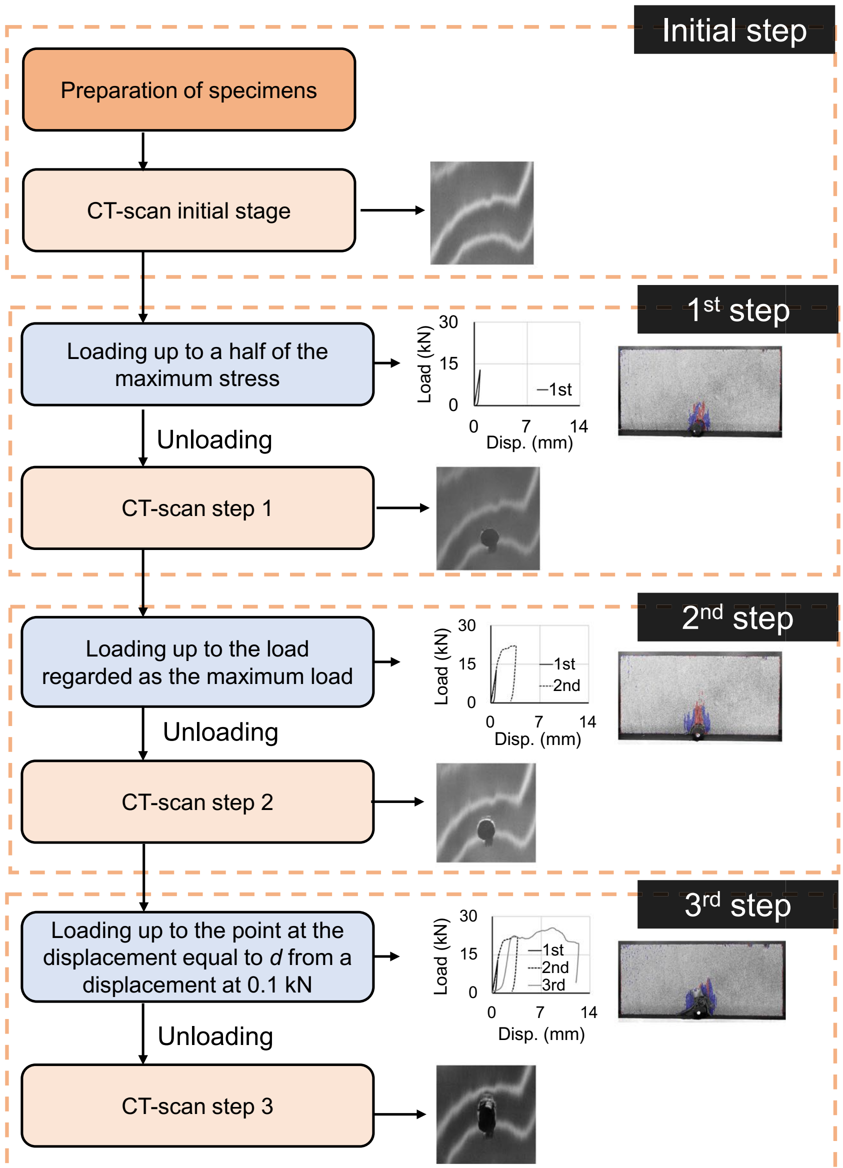

Fig. 2 Schematic of the testing procedure. The specimen is plywood tested along the strong axis (PW-s) with dowel diameter $d = 12$ mm

DIC can obtain the strain contours on the specimen surfaces and the strain distributions along the designated lines but the strain scale was difficult to configure because the boundary of the strongly deformed area was not clearly defined. As the yield strains and other characteristic strain points differ among wood-based panels with different properties, an appropriate and objective standard was difficult to set. The present study proposes an analysis method to resolve these problems.

Figure 9 is a schematic of the analysis process. The analysis focuses on the strain distributions within the range $1d$ –$2d$ from the right and left edges along the middle horizontal line and from the upper edge along the middle vertical line, which are considered to be unaffected by embedding stress. Second, the average μ and standard deviation σ of the strains were calculated in that range. Third, $\mu + 3\sigma$ and $\mu - 3\sigma$ were configured as higher and lower standards, respectively. The lengths of the areas with strains above $\mu + 3\sigma$ and below $\mu - 3\sigma$ were measured and defined as the tensile and compressive strain ranges, respectively. AS the only absolute value of the shear strain was calculated, lengths exhibiting strains above $\mu + 3\sigma$ (defined as the shear strain range) were measured. The lengths of the missing areas in the strain distribution (defined as failure areas) were also measured. Finally, all lengths were divided by d to obtain standardized strain

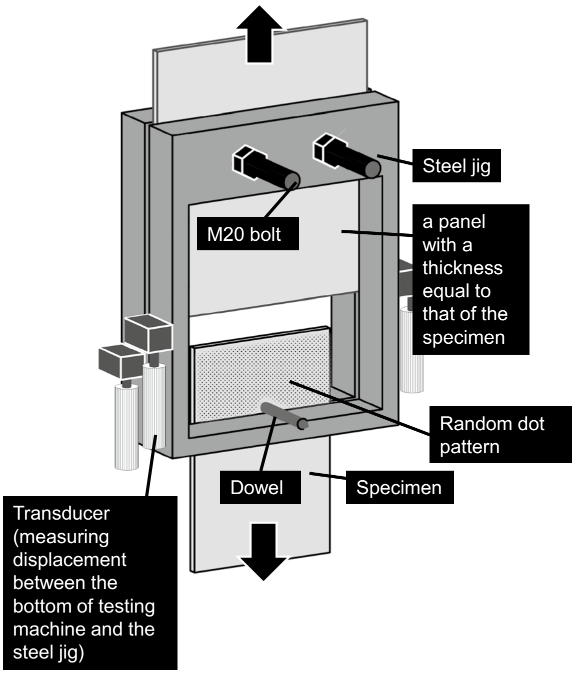

Fig. 3 Schematic of the embedment test

Table 2 One-half of the maximum stress predicted based on our earlier study [1]

Material	*d* (mm)	Predicted one-half of the maximum stress (MPa)
PW-s	5.2	15.0
	12	12.7
PW-w	5.2	21.6
	12	12.5
OSB-s	5.2	20.3
	12	11.6
OSB-w	5.2	20.9
	12	12.8

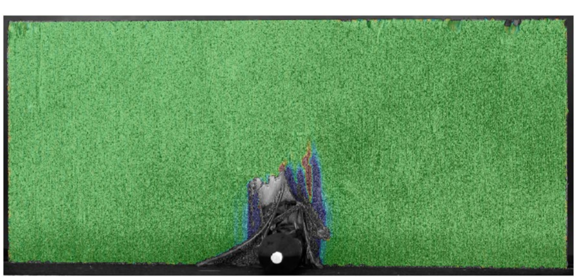

Fig. 4 Contours of strain distribution obtained by the DIC procedure

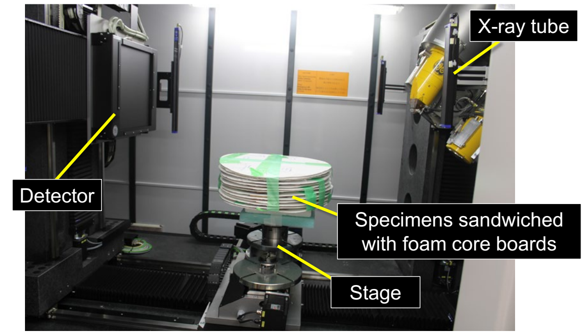

Fig. 5 Schematic of the CT scanning test

ranges. The area within 0.5 d from the edge was not targeted because an erroneously high strain was measured there. This procedure was carried out for each strain type on each specimen.

Comparison of standardized strain ranges and strain-distribution shapes

Figures 10 and 11 compare the standardized strain ranges along the horizontal and vertical lines, respectively. The overall trends exhibited three distinct characteristics. First, the standardized strain range widened during each loading step, particularly along the horizontal lines. Second, the range diminished when the dowel diameter increased. Third, the range spread vertically and horizontally along the strong and weak axes, respectively. The difference between the strong and weak axial specification was more obvious in PW than in OSB. The first, second, and third of these characteristics support the second, third, and fourth of the above hypotheses, respectively.

To understand the stress distributions in the specimens, Figs. 12, 13, 14, and 15 show the strain-distribution contours of PW-s, PW-w, OSB-s, and OSB-w, respectively. In PW-s, the range of vertical x strains was positive in the central area and negative in the side areas, implying that the fiber was ruptured above the dowel and concentrated on both sides of the dowel. This mechanism caused compressive stress in the side section. In previous DIC-based studies on timbers, Lederer [20], who performed a compressive-type embedding test, observed compressive strain over a large area whereas Sjödin, who performed a tensile-type embedding test, did not [8]. As a specimen is usually more ductile under a compressive test than under a tensile test, we surmised that the compressive stress-area side of the dowel is related to ductility. Although a tensile type test was adopted in the present study, the PW-s exhibited ductile behavior under the embedding stress, consistent with our previous study [1]. Therefore, the large compressive stress area observed in the present study might accompany ductile behavior.

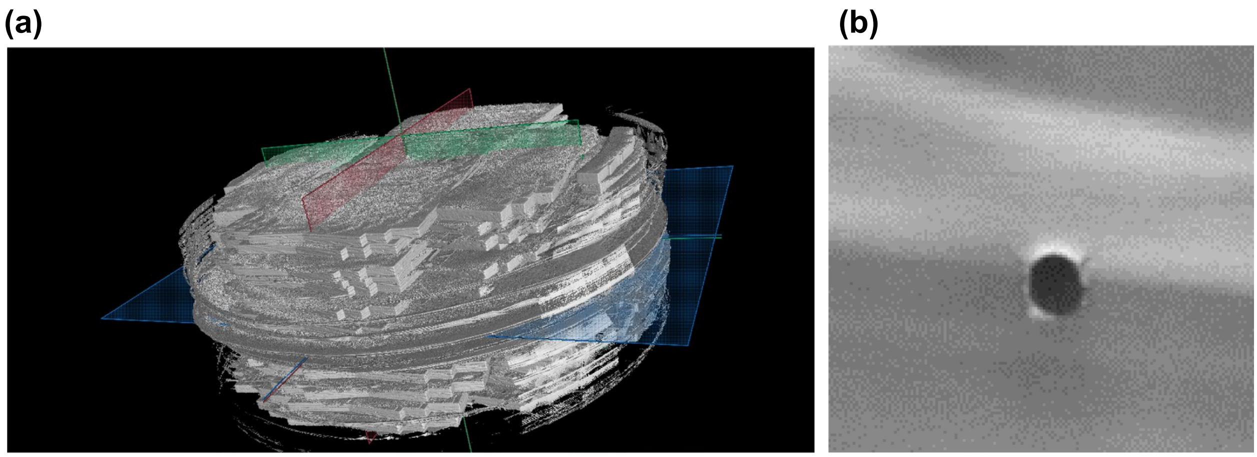

Fig. 6 Grayscale images obtained by the CT scanning apparatus. **a** 3D image and **b** cross-sectional image

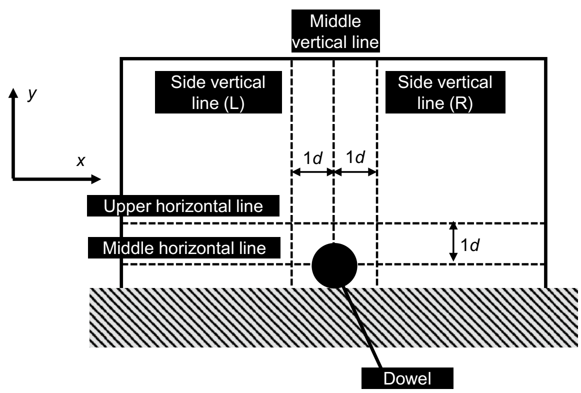

Fig. 7 Targeted lines for the DIC measurements

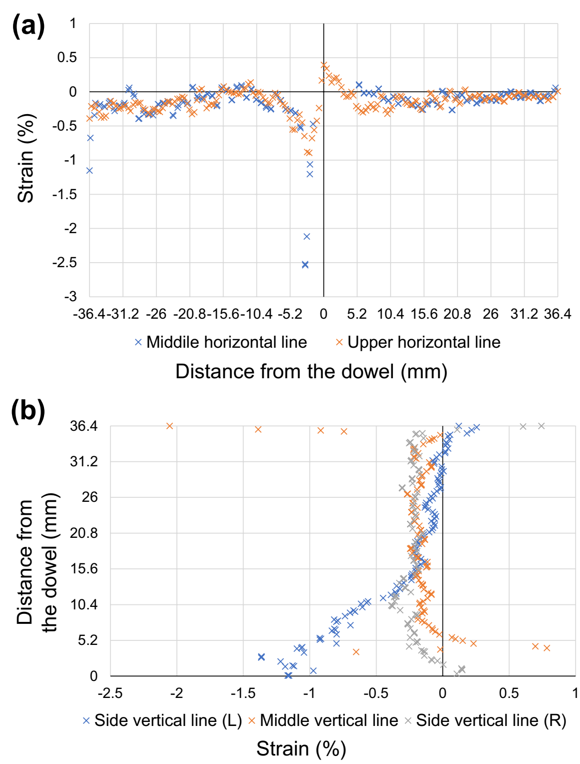

Fig. 8 Representative strain distributions obtained by DIC. **a** Along a horizontal line and **b** along a vertical line. These strain distributions show the *x* strain in PW-s with $d = 5.2$ mm at the second step

In addition, the strain range was widened both horizontally and vertically during each loading step.

The strain distribution in PW-w is characterized by an extensive horizontally spreading *y*-strain, resembling the stress distribution when timber is partially compressed perpendicular to the grain (PCPG) [26, 27]. The substantial variation with *d* is likely attributed to the constant absolute extent of stress spreading, which is independent of pressure area. The strain range was broadened horizontally during each loading step but no broadening was observed at vertical directions, suggesting that the embedding depth remained constant in each step. In addition, the shear strain along the horizontal lines was minimally expanded during each loading step (see Fig. 10) and the shear strain was smaller along the central vertical line than along the side vertical line. Figure 16 plots the *y*-strain and shear strain along the upper horizontal line of PW-w. The shear strain peaked at the position of bottom of *y*-strain, implying that the shear strain range located at the boundary of the *y*-strain range. The width of this boundary line did not expand, even when the range of *y* strains widened.

In OSB, the strains did not differ between the strong and weak axial specifications obviously, and they substantially depended on *d*. During each loading step, the

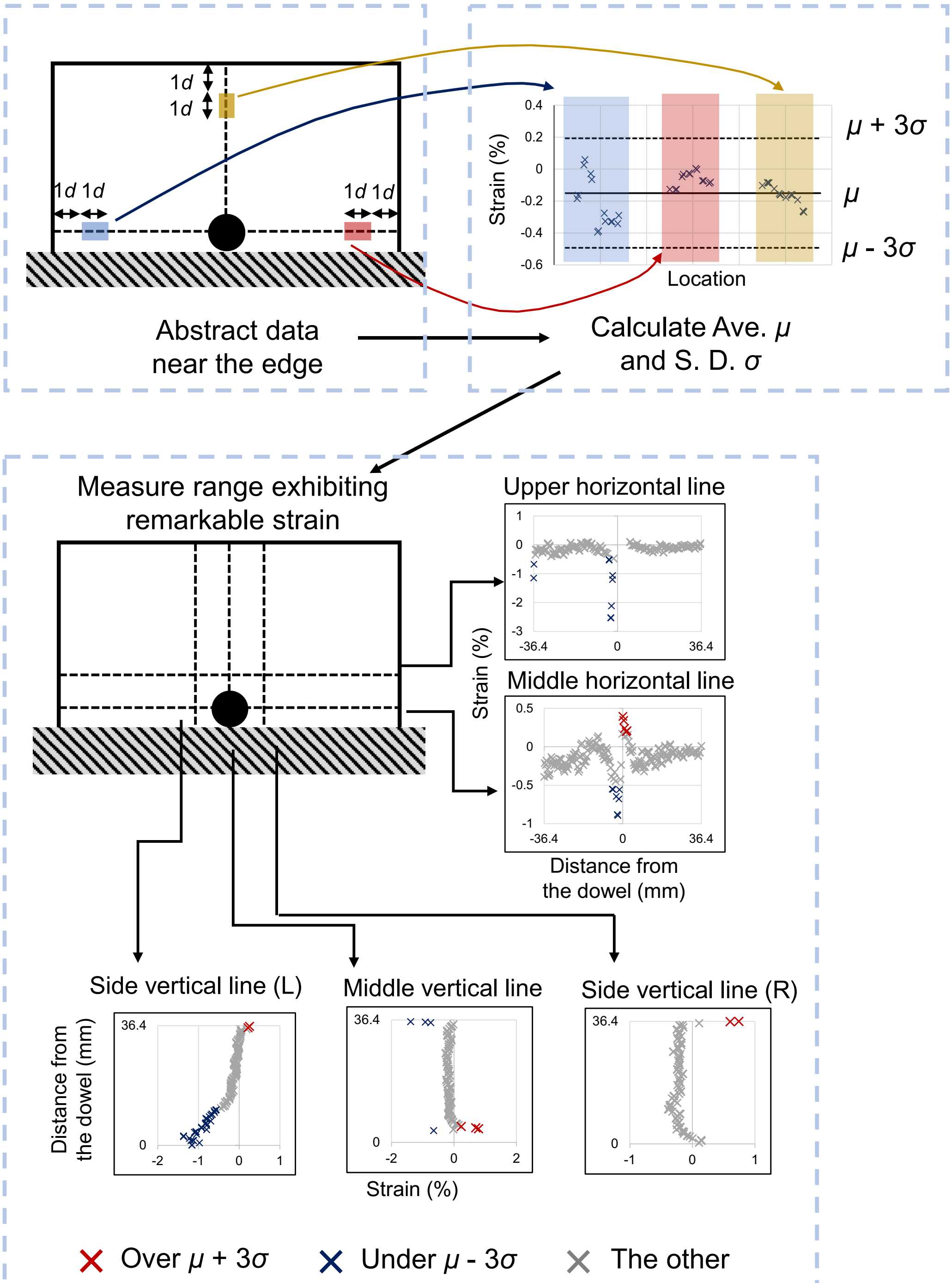

Fig. 9 Schematic showing the analysis of the DIC results

strain range significantly broadened only in the horizontal direction. The x strain was distributed circularly, as shown in Figs. 14 and 15.

CT scanning results

Analysis method

Internal cross-sectional images of five plywood layers and three OSB layers were acquired via CT scanning at the locations shown in Fig. 17. The brightness and contrast at each step were harmonized and the difference

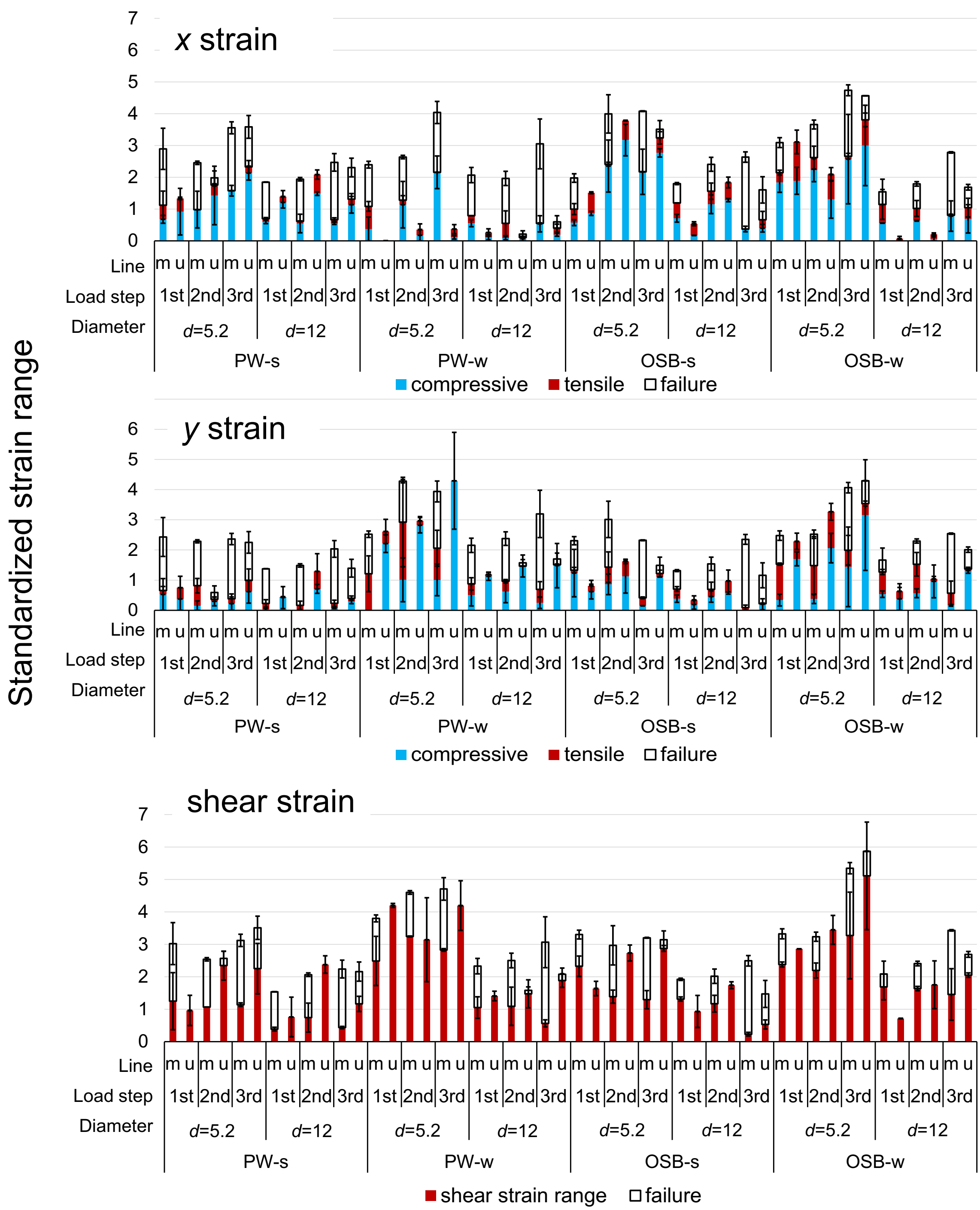

Fig. 10 Comparison of strain ranges along the horizontal lines. "1st", "2nd", and "3rd" denote the test steps. "m" and "u" denote the middle and upper horizontal lines, respectively. Error bars are the standard deviations

images were binarized as demonstrated in Fig. 18. The threshold was determined manually by each specimen based on visual difference image and brightness histogram before binarization to be set as the layer pattern (e.g., annual rings of veneers and the configuration of strands) and the density change were made invisible and visible, respectively, as far as possible. This procedure was conducted by specified one person. The areas voided or densified under the embedding pressure were determined from the brightness differences in the images. The

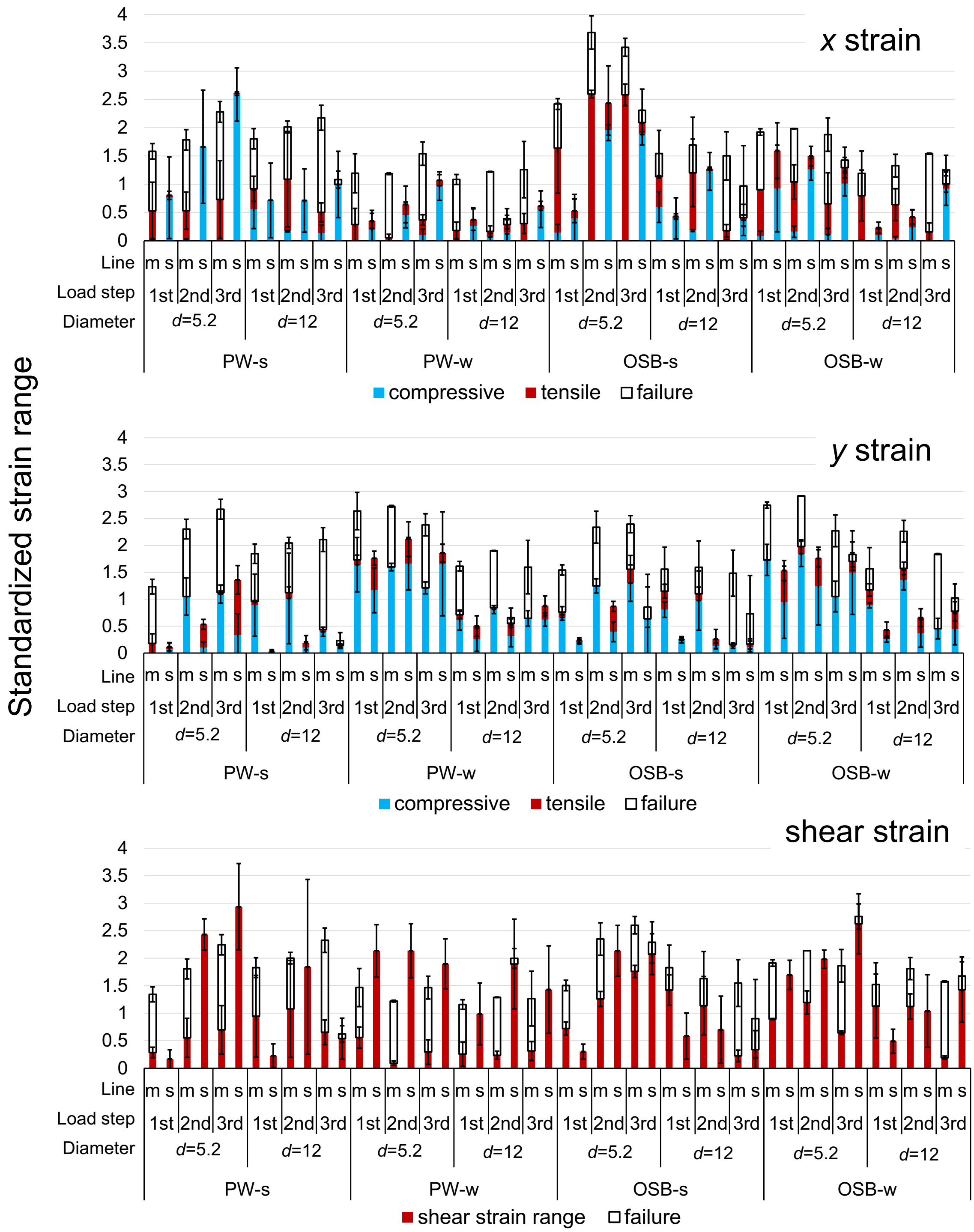

Fig. 11 Comparison of strain ranges along the vertical lines. "1st", "2nd", and "3rd" denote the test steps. "m" and "s" denote the middle and side vertical lines, respectively. Error bars are the standard deviations

first-step–second-step and second-step–third-step difference images were obtained as the plasticity difference (PD) and ultimate difference (UD) images, respectively, for each specimen and each cross-section. In addition, a density distribution in the thickness direction is likely to be taken into consideration when highly homogeneous panels are targeted such as MDF. However, since a layer in PW and OSB is composed of a veneer and strands,

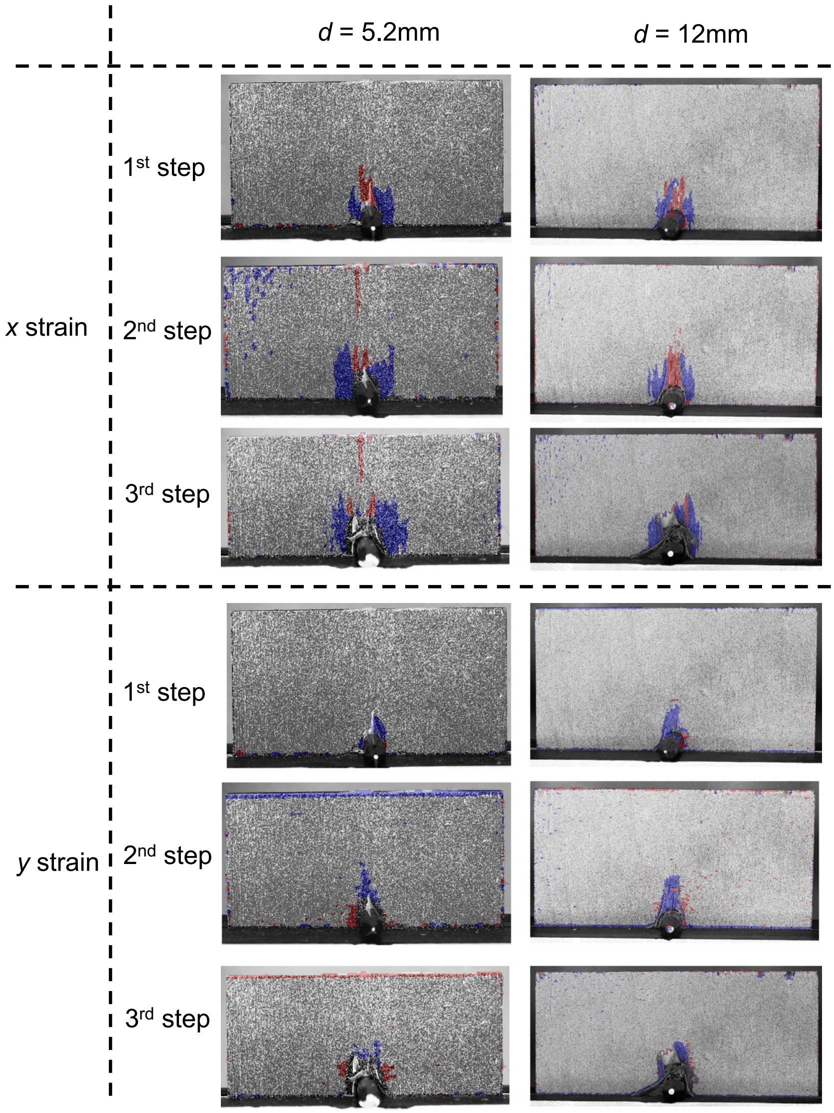

Fig. 12 Contours of strain distributions in PW-s. Red and blue areas indicate where the strains are above $\mu + 3\sigma$ and below $\mu - 3\sigma$, respectively

respectively, the density variation in the in-plane direction is high. Therefore, even if a density distribution in the thickness direction is investigated, whether the density variation is attributed to the density variation in the in-plane or the thickness direction is unclear. For these reasons, a density distribution in the thickness direction was not verified in this study.

In Fig. 19, the voided and densified regions in the derived difference images are categorized as follows: Region A (immediately above the dowel), Region B (left and right of the dowel), Region C (above the dowel), Region D (diagonally above the dowel), and Region E (otherwise). This categorization ascertains the deformed location in each specification, each layer, and each step. After identifying the fracture areas, it was discussed whether a layer with different specifications exhibited similar fracture features. The procedure is detailed below.

We first assessed whether the failure mode depends on the location of the target layer (outer or inner). For this purpose, the first and fifth layers of plywood and the first and third layers of OSB were deemed the outer layers, whereas the third layer of plywood and the second layer of OSB were deemed the inner layers. Table 3 presents the probabilities of density changes occurring under each condition. Figure 20 shows the result of a regression analysis on the data of Table 3, where R^2 indicates the similarity in fracture forms between the outer and inner layers with other

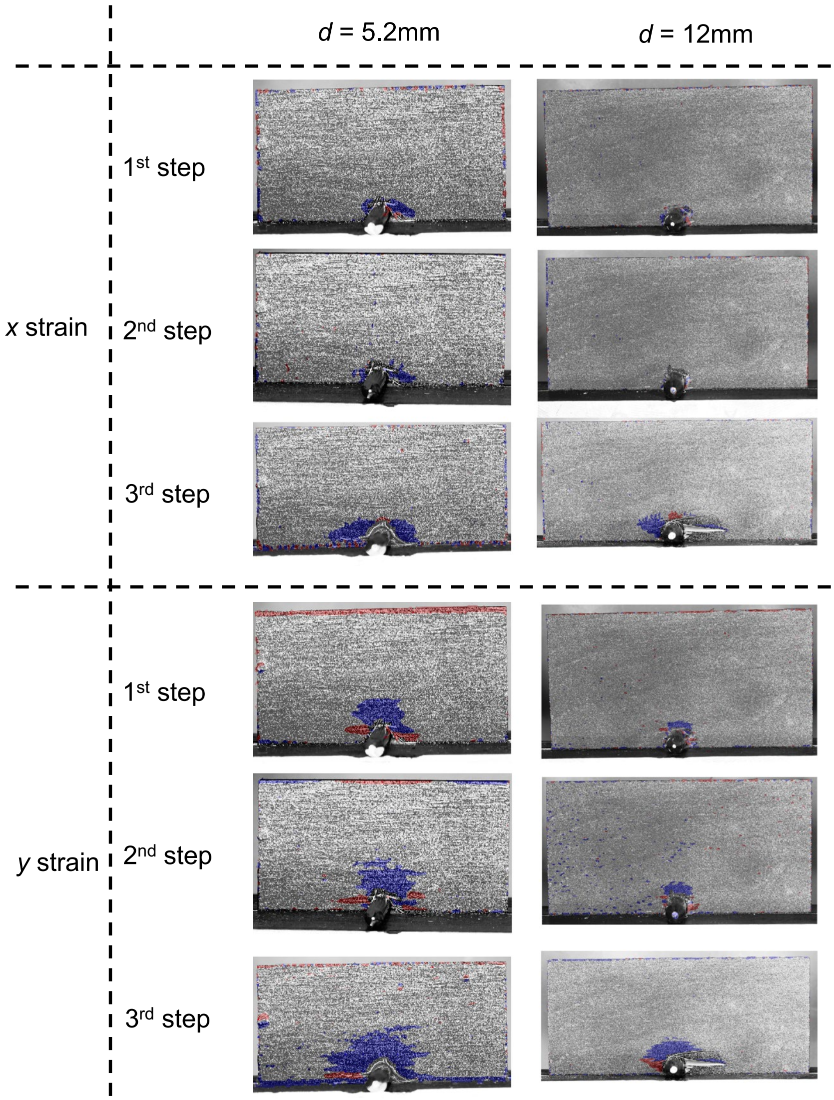

Fig. 13 Contours of strain distributions in PW-w. Red and blue areas indicate where the strains are above $\mu+3\sigma$ and below $\mu-3\sigma$, respectively

conditions matched. This analysis was separately conducted for PW and OSB and for PD and UD, yielding four distinct R^2 values.

Whether the failure modes differed between the strong-axis and weak-axis layers was evaluated similarly. The first, third and fifth layer of PW-s, first and third layer of OSB-s, and the second layer of OSB-w were deemed strong-axis layers, whereas the first, third, and fifth layer of PW-w, the second layer of OSB-s, and the first and third layers of OSB-w were deemed weak-axis layers. The second and fourth layers of PW were ignored to ensure the same conditions as when combining the inner and outer layers. The comparison data (Table 4) were subjected to a regression analysis as described above.

Classification results of failure behavior

The R^2 values of the inner vs. outer layers and strong vs. weak layers are compared in Table 5. In PW, the inner vs. outer comparison yielded higher R^2 values than the strong vs. weak comparison, for both PD and UD. Therefore, the failure mode in this specimen was only slightly affected by layer position but was largely affected by variations in fiber direction.

In OSB, the inner vs. outer layer comparison yielded lower R^2 values than the strong vs. weak layer comparison for UD but the reverse was true for PD. Between the inner vs. outer and strong vs. weak comparisons, the UD varied more widely than PD. The deformation behavior was also more obvious in UD than in PD. Accordingly, the results of UD are regarded as more important than those of PD. The failure behavior of a layer in OSB is

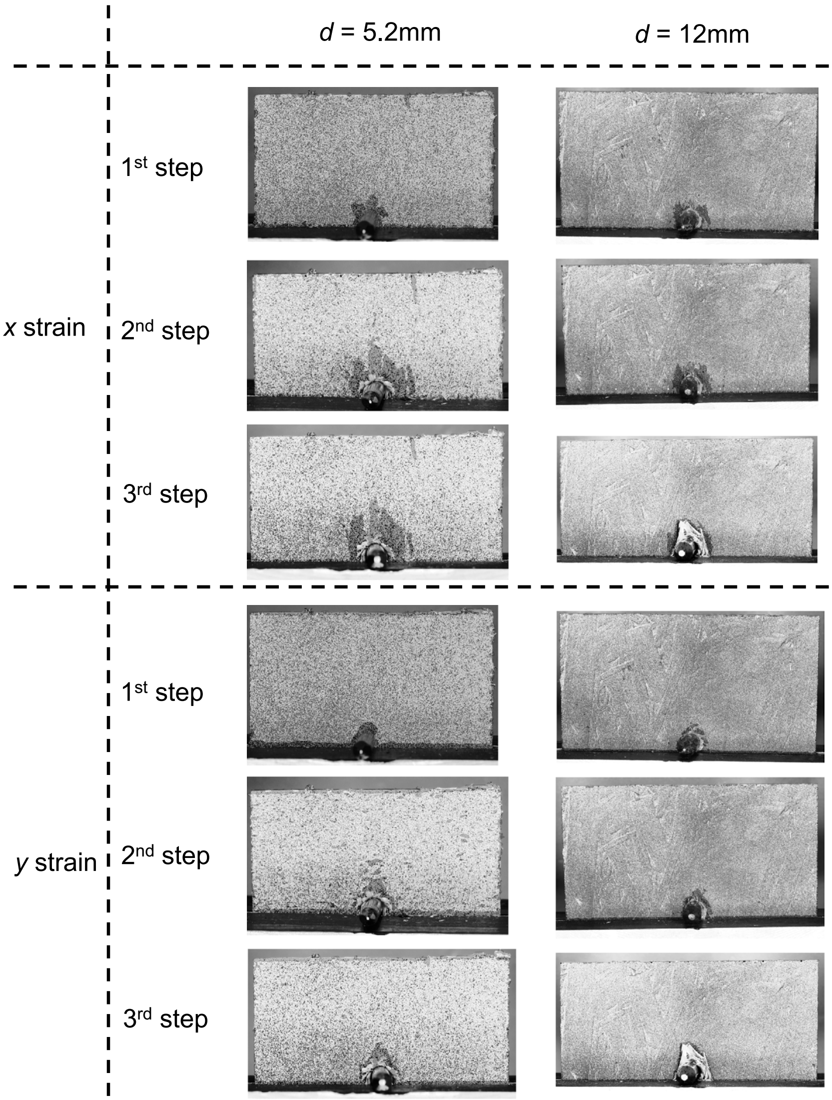

Fig. 14 Contours of strain distributions in OSB-s. Red and blue areas indicate where the strain is above $\mu + 3\sigma$ and below $\mu - 3\sigma$, respectively

probably dominated by the position rather than the fiber direction of the layer. This discussion aligns with the first hypothesis in our earlier study.

Moreover, the fibers in the odd-numbered veneer layers (first, third and fifth layers) of PW-s were oriented identically to the even-numbered veneer layers (second and fourth layers) of PW-w. Additionally, the even-numbered veneer layers of PW-s and the odd-numbered veneer layers of PW-w were identical in the fiber direction. Adopting a common analysis method, we then determined whether the different fracture form was exhibited by the variation between the odd- and even-numbered layers as the fiber direction was matched. The R^2 values were 0.82 and 0.80 for the PD and UD cases, respectively, demonstrating that the failure behavior in PW was determined only by the direction of the veneer fibers, independently of layer position.

Density changes in each region and comparison among their size

Table 6 presents the probabilities of density changes in each specification. Figure 21 shows representative difference images of strong and weak axial layers in PW and the outer and inner layers in OSB.

Position B was commonly densified in the strong axial layers of PW, possibly because the fibers on both sides of the dowel were condensed by fiber dissociation from the center. Both voids and densification were observed at location C in the UD image, likely because cracks propagated upward during large deformations.

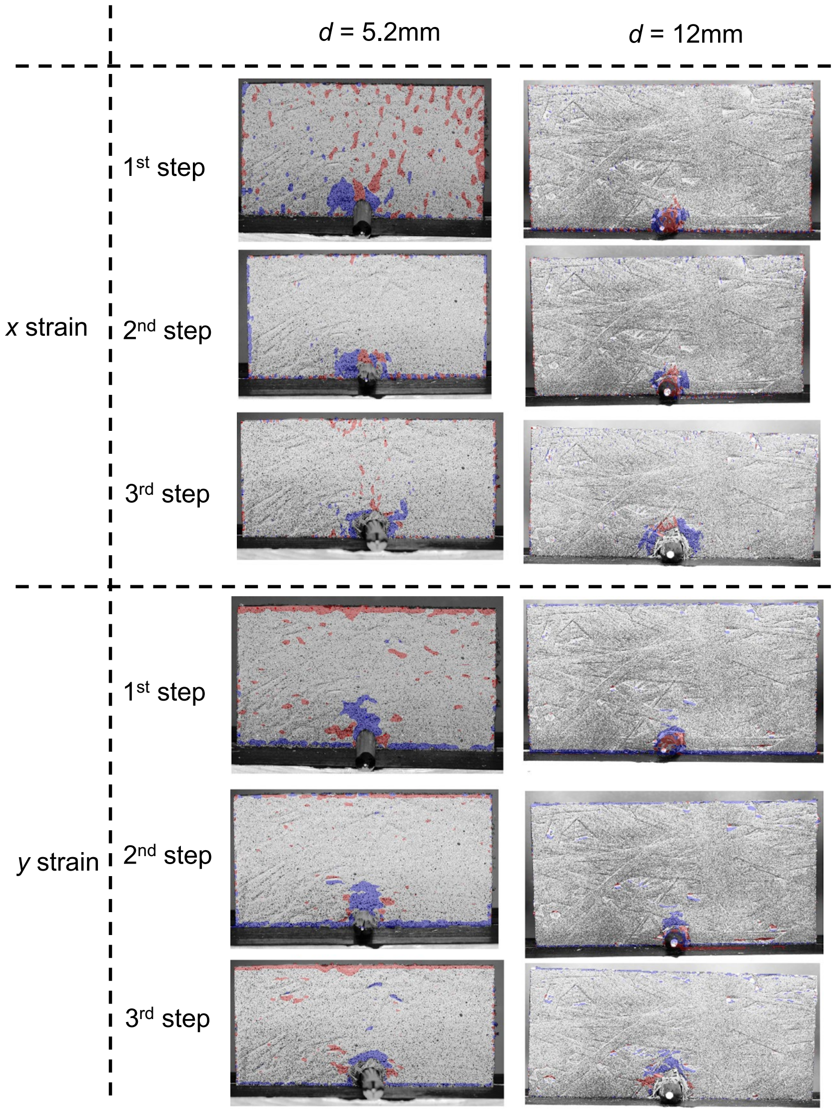

Fig. 15 Contours of strain distributions in OSB-w. Red and blue areas indicate where the strain is above $\mu+3\sigma$ and below $\mu-3\sigma$, respectively

Areas C and D in the weak axial layer of the UD experienced voiding and densification when the layer was deformed by embedding stress and became plasticized and fractured above, to the right, and to the left of the dowel. The deformation failed to recover after unloading.

Voids in areas B, C, D, and E were largely distributed and scattered through the outer layer of OSB, presumably resulting from surface delamination. Only the inner layer of OSB was densified, and voiding and densification frequently appeared in area C. These findings suggest that out-of-plane delamination predominates in the outer layer, whereas in-plane compressive deformation predominates in the inner layer.

The voided and densified areas were standardized by dividing each area by the dowel size. The results are shown in Fig. 22. After increasing the dowel diameter, the densified area decreased but the void area showed no significant change (in contrast, the void area in the strong axial layer of PW was widened by increasing *d*). As the void area included the movement trace of the dowel, its absolute size varied proportionally with diameter. The results of the densified areas were consistent with the third hypothesis in our earlier study at least. In PW, the weak axial layer exhibited a larger densified and void area than the strong axial veneer, probably because the densification of the region to the left and right of the dowel due to fiber dissociation was indirectly caused by stress

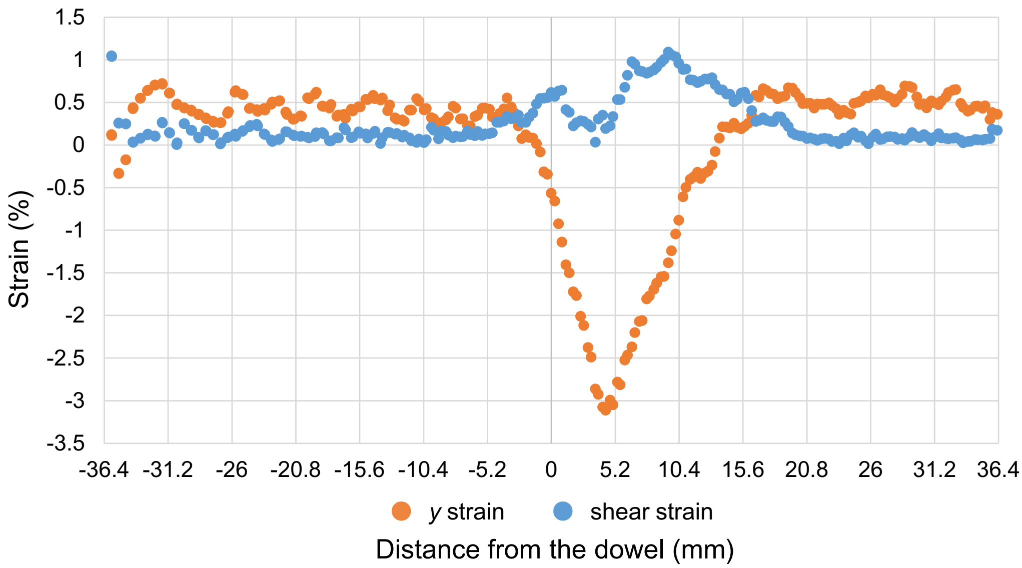

Fig. 16 *y*-axis and shear strains versus distance from dowel. Strain distributions were measured along the upper horizontal line of PW-w with $d = 5.2$ mm at the third step

acting perpendicular to the direction of the applied force in the strong axial layer. Conversely, embedment into the weak axial veneer is directly caused by stress acting parallel to the applied force. A large void area and a certain sized densified area were observed in the outer and inner layer of OSB, respectively. Therefore, it can be concluded that embedment stress in OSB causes delamination in the surface layer and compressive deformation in the inner layer. In addition, the standardized void area of the surface layer depended on the diameter, although the standard deviations are wide. In other words, the absolute value of the delamination area is apparently independent of diameter.

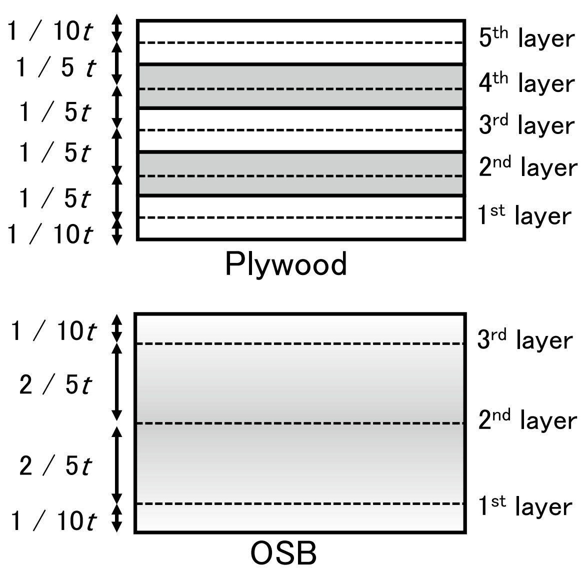

Fig. 17 Targeted cross sections in the CT-based analysis. *t* denotes the thickness of the wood-based panel

Discussion

The strain distributions and deformation behavior determined from the DIC and CT scanning results were consistent. Additionally, most of the results support the hypotheses proposed in our earlier study. Therefore, the failure behavior of PW and OSB was reliably elucidated. Based on the results, we now discuss a theoretical model of the failure behavior under embedding stress.

A horizontal tensile strain is generated at the middle vertical line of the strong axial layer in PW, causing lateral compression to the right and left of the dowel. A previous study adopted fracture mechanics to explain the brittle splitting in timber under an embedding stress parallel to the grain [8]. However, fracture mechanics seems inappropriate for predicting the embedding strength of the strong axial layer because the failure mode of PW is ductile. Previous studies on timber [28, 29] discussed and established theoretical models of lateral stress at the side of the dowel. These models might (at least in part) also explain the strong axial layer in PW.

The failure behavior of the weak axial layer in PW under embedding stress is similar to that of timber under PCPG, as the *y* compressive strain is horizontally distributed and the densified area is located diagonally above the dowel. Whereas fracture mechanics is assumed in timber loaded perpendicular-to-grain [30,

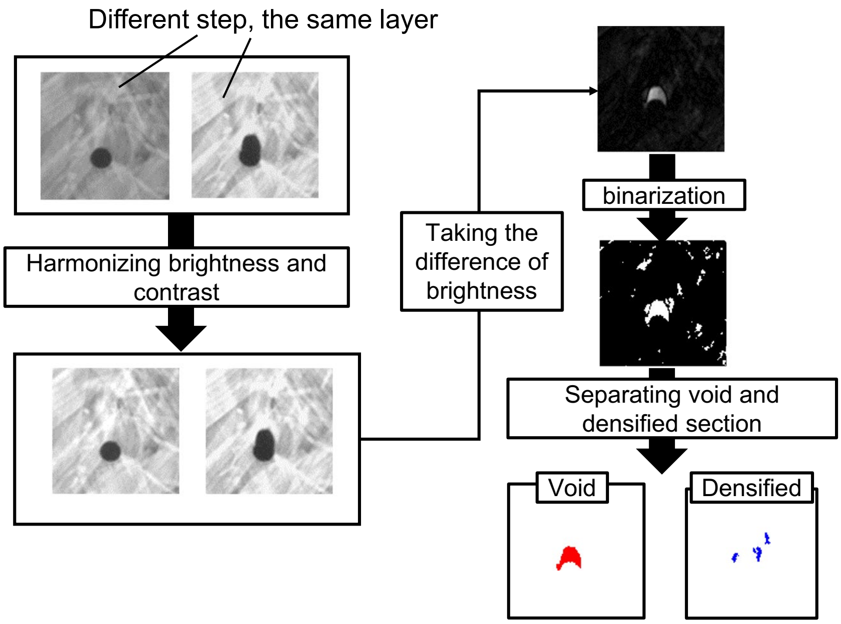

Fig. 18 Schematic showing the method for analyzing density changes

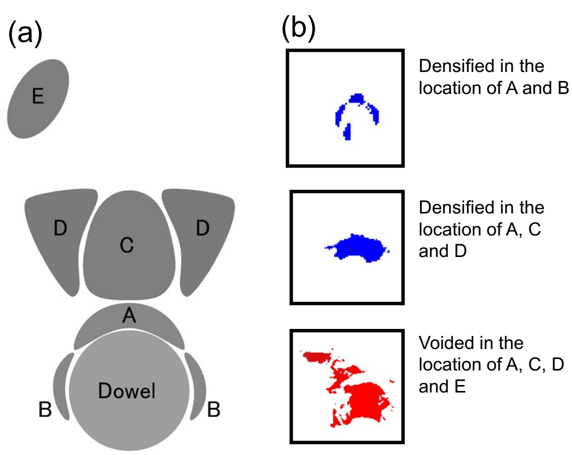

Fig. 19 Categorization of voided and densified areas. **a** Location of each categorized area; **b** examples of categorization

31], PCPG theory (applied to timber loaded parallel-to-grain) is possibly applicable to the weak axial layer in PW under an embedding stress.

Although the embedding performance of PW approximately equals the summed performances of the individual layers, adhesive layers might also contribute. The adhesive layer, which binds the deformations of two adjacent layers with different fiber directions and fracture behaviors (the so-called locking effect [32]), will likely resist embedding stress. These effects should be quantitatively evaluated in future study.

As the outer and inner layers in OSB are fractured in different ways, their behavior must be modeled for estimating the embedding performance of OSB. However, the delamination of wood-based panels generated by in-plane compressive stress has not been reported. Although this phenomenon appears to be related to Poisson's effect or buckling, a theoretical model is required in further work. Developing such a model is difficult because very few studies have explored this type of failure behavior.

Conclusion

This study reported the detailed strain distributions and failure behaviors of wood-based panels using the DIC and CT scanning techniques. PW and OSB were selected as representative panels. One aim of this observation was to verify the hypotheses obtained in our earlier study: (i) there exist two types of failure behavior (in-plane failure and out-of-plane failure) when the edge distance is sufficient; (ii) the stress-spreading range is larger at the maximum stress than at the yield stress; (iii) the stress-spreading range (normalized by the dowel diameter) reduces when the dowel diameter increases; and (iv) the stress generated by embedment pressure preferentially spreads vertically and horizontally along the strong and

Table 3 Comparisons of failure behavior between the outer and inner layers

Direction	Diameter (mm)	Voided or densified	Probability of density change in	Outer	Inner
Strong	5.2	Voided	A	1	1
			B	0.5	0.5
			C	0.5	1
			D	0	0
			E	0	0
		Densified	A	1	1
		…	…	…	…
	12	Voided	A		
		…	…		
		Densified			
		…			
Weak	5.2	Voided	A		
…	…	…	…		

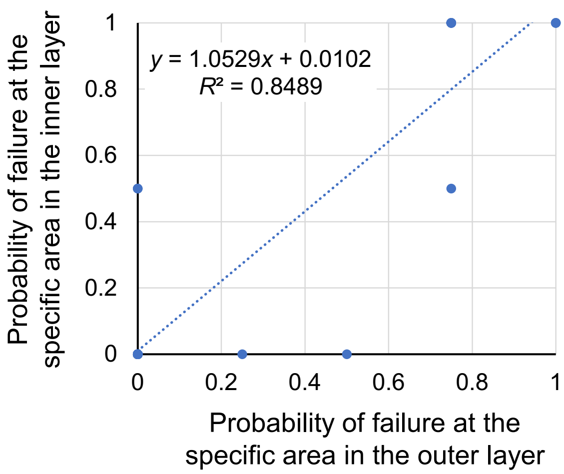

Fig. 20 Representative regression analysis of fracture probability

Table 4 Comparisons of failure behavior between the strong and weak axial layers

Position	Diameter (mm)	Voided or densified	Probability of density change in	Strong	Weak
Outer	5.2	Voided	A	1	1
			B	0.5	0.5
			C	0.5	1
			D	0	0.5
			E	0	0.25
		Densified	A	1	1
		…	…	…	…
	12	Voided	A		
		…	…		
		Densified			
		…			
Inner	5.2	Voided	A		
…	…	…	…		

weak-axis specifications, respectively. Whether each hypothesis is supported or not supported is discussed below.

Table 5 Comparison of R^2 values

Comparison	Material	Step	R^2
Inner vs. outer	PW	PD	0.85
		UD	0.66
	OSB	PD	0.66
		UD	0.38
Strong vs. weak	PW	PD	0.61
		UD	0.24
	OSB	PD	0.55
		UD	0.53

"Inner vs outer" and "Strong vs Weak" indicate the correlations between outer and inner layers and between strong and weak axial layers, respectively. PD and UD mean plastic difference and ultimate difference, respectively

Hypothesis (i)—accepted

From the CT scanning results, the panel layers were classified based on densified or voided locations around the dowel. Consequently, the layers in PW were classified into strong and weak axial layers and those in OSB were classified into outer and inner layers.

Table 6 Comparisons of density-change probabilities in each region

Layer	*d* (mm)	Step	Change in density	A	B	C	D	E
(a)								
Strong	5.2	PD	Void	**0.9**	0.2	0	0	0
			Densified	**0.9**	**0.6**	0	0	0
		UD	Void	**1**	0.4	**0.8**	0	0
			Densified	**1**	**0.9**	**0.6**	0	0
	12	PD	Void	**1**	0	0	0	0.1
			Densified	**1**	0.1	0	0	0
		UD	Void	**1**	0.4	**0.7**	0.2	0.3
			Densified	**1**	**0.5**	**0.5**	0.1	0.1
Weak	5.2	PD	Void	**0.8**	0.3	0.2	0.2	0
			Densified	**0.9**	0	0	0	0
		UD	Void	**1**	0.3	**1**	**0.9**	0.3
			Densified	**0.9**	0.2	**1**	**0.7**	0.1
	12	PD	Void	**1**	0	0	0	0
			Densified	**0.9**	0.1	0	0	0
		UD	Void	**1**	0.1	**1**	**0.5**	0.3
			Densified	**1**	**0.6**	**0.8**	**0.5**	0.1
(b)								
Outer	5.2	PD	Void	**1**	0.125	0.375	0.25	0.125
			Densified	**0.5**	0.25	0	0.25	0.125
		UD	Void	**1**	**0.625**	**0.875**	**0.625**	**0.75**
			Densified	**0.5**	0.125	0.125	0.25	0.25
	12	PD	Void	**1**	0	0	0	0.125
			Densified	0.375	0	0	0	0
		UD	Void	**1**	0	0	0	0.125
			Densified	0.375	0	0	0	0
Inner	5.2	PD	Void	**1**	0.25	**0.5**	0.25	0.25
			Densified	**0.75**	0	0.25	0.25	0
		UD	Void	**1**	**0.5**	**0.75**	0.25	0.25
			Densified	**0.75**	0	**0.5**	**0.75**	0
	12	PD	Void	**1**	0	0.25	0.25	0
			Densified	**1**	0	0	0	0
		UD	Void	**0.75**	0	**0.75**	**0.5**	0
			Densified	**0.75**	0	**0.5**	0.25	0

(a) PW and (b) OSB. Values ≥ 0.5 are highlighted in bold font

Hypothesis (ii)—intermediately accepted

The DIC results revealed a high-strain range that increased along the horizontal direction for each strain type in each panel except for shear strain in PW-w. In contrast, the high-strain range along the vertical direction increased only in PW-s.

Hypothesis (iii)—intermediately accepted

When the dowel diameter increased, the DIC results revealed a decrease in the standardized strain range, whereas the CT scanning results showed a decrease in the standardized densified areas but no decrease in the void areas.

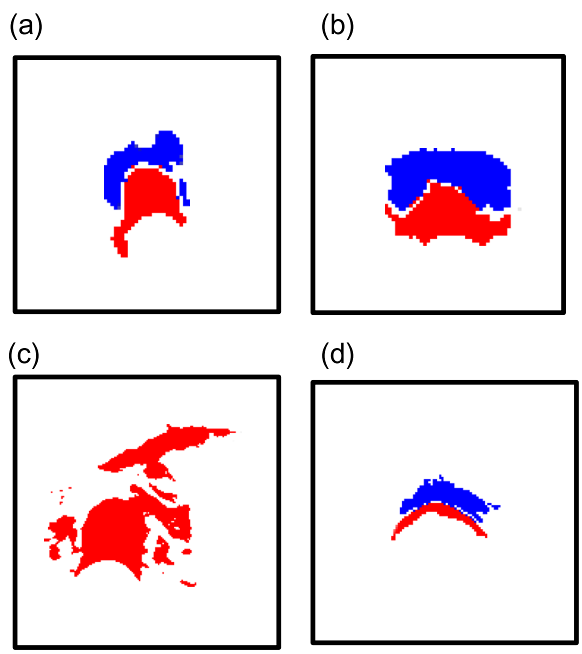

Fig. 21 Representative difference images exhibiting voided and densified areas. Red and blues areas are voided and densified areas, respectively. **a** Image of a strong axial layer in PW (ultimate difference (UD) of the third layer of PW-s with $d = 5.2$ mm). **b** Image of a weak axial layer in PW (UD of the fourth layer of PW-s with $d = 5.2$ mm). **c** Image of an outer layer in OSB (UD of the first layer of OSB-w with $d = 12$ mm). **d** Image of an inner layer in OSB (plasticity difference of the second layer of OSB-s with $d = 12$ mm)

Hypothesis (iv)—accepted

The strain range spread vertically and horizontally along the strong and weak axial specifications, respectively.

In summary, the results of DIC and CT scanning roughly supported the above hypotheses.

The failure behaviors of the strong and weak-axis specifications strongly differed in PW but not in OSB. The fibers at both sides of the dowel in the strong axial layer of PW were densified under an embedding stress because the fibers dissociated immediately above the dowel. The weak axial layer in PW was deformed like the timber partially compressed perpendicular-to-grain. The outer layer in OSB under an embedding stress exhibited a circularly distributed strain range and a dispersed void area. Densified areas appeared only in the inner layer of OSB.

These findings will likely contribute to a theoretical model of the embedding performance of wood-based panels. The obtained strain ranges provide an evidence for connecter configurations such as edge distance, end distance, and distance between connecters. The revealed failure behavior may assist the development and improvement of manufacturing methods for wood-based panels with increased embedding performance. Further studies are needed to fully realize these goals.

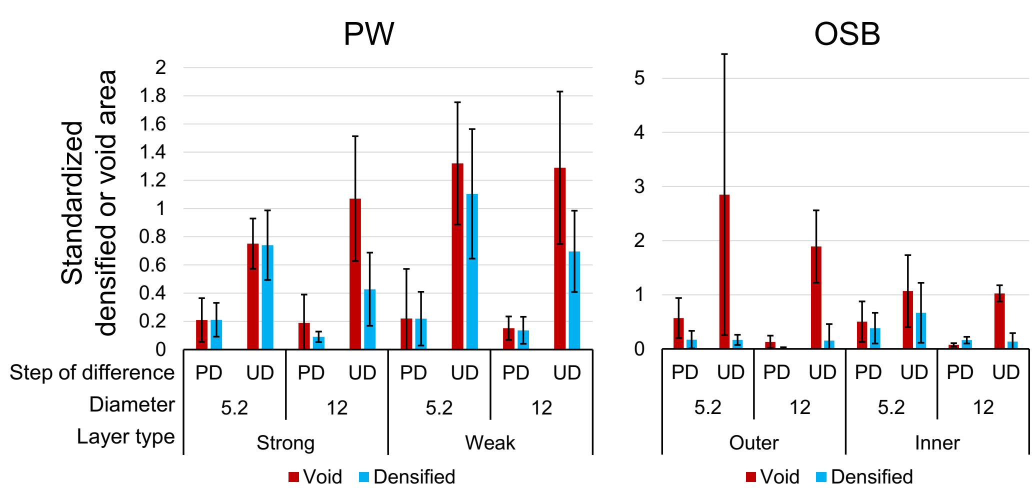

Fig. 22 Comparisons of standardized area densities. Error bars indicate standard deviation

Abbreviations

PW Plywood
OSB Oriented strand board
DIC Digital image correlation
CT Computed tomography

Acknowledgements

The plywood used in this study was supplied by SEIHOKU corporation. The authors acknowledge the Japan Wood Research Society for providing the Article Processing Charge of this article. We are deeply grateful to all those who were involved. This report was presented partially at the Annual Meeting of Japan Wood Research Society Kyusyu (2023), Fukuoka, March 2023, the Annual Meeting of AIJ Hokkaido (2022), Sapporo, September 2022, and the 16th World Conference on Timber Engineering, Oslo, Kingdom of Norway, June 2023.

Author contributions

RS designed and performed the experiments, analyzed the data, and largely contributed to the writing of the manuscript. All authors contributed to the interpretation and discussion of the results. All authors have read and approved the final manuscript.

Funding

This study was supported by a Grant-in-Aid for JSPS Research Fellow (no. 20J20611). This work was also supported by The International Exchange Encouragement Award from the Japan Wood Research Society through JSPS KAKENHI, Grants-in-Aid for Publication of Scientific Research Results (JP 22HP2003).

Availability of data and materials

The datasets used and analyzed in the current study are available from the corresponding author upon reasonable request.

Declarations

Competing interests

The authors declare that they have no competing interests.

Received: 19 September 2023 Accepted: 17 November 2023
Published online: 27 November 2023

References

1. Sudo R, Aoki K, Inayama M (2023) Investigation of mechanical properties and elucidation of factors affecting wood-based structural panels under embedment stress with a circular dowel i: analysis of the influence of various conditions on the embedment properties. J Wood Sci 69(18):1–5. https://doi.org/10.1186/s10086-023-02093-2
2. Murata K, Masuda M, Ichimaru M (1999) Analysis of radial compression behavior of wood using digital image correlation method. Mokuzai Gakkaishi 45(5):375–381
3. Inoue S, Muramoto M (2023) Measuring the elastic-plastic surface displacement of partially compressed wood and evaluation of partial compressive load perpendicular to the grain. J Struct Eng (AIJ) 88(805):467–478. https://doi.org/10.3130/aijs.88.467
4. Totsuka M, Jockwer R, Aoki K, Inayama M (2021) Experimental study on partial compression parallel to grain of solid timber. J Wood Sci. https://doi.org/10.1186/s10086-021-01972-w
5. Ukyo S, Hayashi T, Harada M, Karube M (2007) Effect of longitudinal shear plane length on the tensile strength of half-lapped "gooseneck" splice joints (kama-tsugi)—strain distribution analysis of the tenon using digital image correlation. Mokuzaigakkaishi 53(2):90–98. https://doi.org/10.2488/jwrs.53.90
6. Sjödin J, Enquist B, Serrano E (2006) Contact-free measurements and numerical analyses of the strain distribution in the joint area of steel-to-timber dowel joints. Holz Roh Werkst 64(6):497–506. https://doi.org/10.1007/s00107-006-0112-1
7. Shi D, Demartino C, Li Z, Xiao Y (2023) Axial load–deformation behavior and fracture characteristics of bolted steel to laminated timber and glubam connections. Dig Compos Struct. https://doi.org/10.1016/j.compstruct.2022.116486
8. Sjödin J, Serrano E, Enquist B (2008) An experimental and numerical study of the effect of friction in single dowel joints. Holz Roh Werkst 66(5):363–372. https://doi.org/10.1007/s00107-008-0267-z
9. Schoenmakers JCM (Dennis), Svensson S (2011) Embedment tests perpendicular to the grain—optical measurements of deformation fields. Dig Eur J Wood Wood Prod 69(1):133–142. https://doi.org/10.1007/s00107-009-0404-3
10. Ukyo S, Masuda M (2003) Strain analysis of wood around drift-pin joints using the digital image correlation method. Mokuzaikkaishi 49(3):197–204
11. Jeong GY, Kong JH, Lee SJ, Pang S-J (2018) Comparisons of bearing properties for various oriented glulam using digital image correlation. J Wood Sci 64(3):237–245. https://doi.org/10.1007/s10086-018-1700-5
12. Lindgren O, Seifert T, Du Plessis A (2016) Moisture content measurements in wood using dual-energy CT scanning—a feasibility study. Wood Mater Sci Eng 11(5):312–317. https://doi.org/10.1080/17480272.2016.1201863
13. Brodersen CR (2013) Visualizing wood anatomy in three dimensions with high-resolution X-ray micro-tomography (μCT)—a review. IAWA J 34(4):408–424. https://doi.org/10.1163/22941932-00000033
14. De Ligne L, De Muynck A, Caes J, Baetens JM, De Baets B, Van Hoorebeke L, Van Acker J, Van den Bulcke J (2022) Studying the spatio-temporal dynamics of wood decay with X-ray CT scanning. Holzforschung 76(5):408–420. https://doi.org/10.1515/hf-2021-0167
15. Zauner M, Keunecke D, Mokso R, Stampanoni M, Niemz P (2012) Synchrotron-based tomographic microscopy (SbTM) of wood: development of a testing device and observation of plastic deformation of uniaxially compressed Norway spruce samples. Holzforschung 66:973–979. https://doi.org/10.1515/hf-2011-0192
16. Forsberg F, Mooser R, Arnold M, Hack E, Wyss P (2008) 3D micro-scale deformations of wood in bending: synchrotron radiation muCT data analyzed with digital volume correlation. J Struct Biol 164(3):255–262. https://doi.org/10.1016/j.jsb.2008.08.004
17. Adams AR (2009) Quantitative radiographic investigations of mechanical fasteners in wood connections. Masters Thesis. The Pennsylvania State University.
18. Shinohara T, Kobayashi K, Tanaka K (2019) The evaluation of the withdrawal performance of the inclined screw inserted in CLT. Abstracts of the annual meeting of Japan wood research, Hakodate-arena, Hokkaido, D14-01-1400 March 2019.
19. Keunecke D, Novosseletz K, Lanvermann C, Mannes D, Niemz P (2012) Combination of X-ray and digital image correlation for the analysis of moisture-induced strain in wood: opportunities and challenges. Eur J Wood Wood Prod 70(4):407–413. https://doi.org/10.1007/s00107-011-0573-8
20. Lederer W, Bader TK, Muszyński L, Eberhardsteiner J (2016) Exploring a multi-modal experimental approach to investigation of local embedment behaviour of wood under steel dowels. Strain 52:531–547. https://doi.org/10.1111/str.12199
21. Japanese Agricultural Standard (2014) JAS for plywood. Japanese Agricultural Standards Association, Tokyo
22. Japanese Agricultural Standard (2013) JAS for OSB. Japanese Agricultural Standards Association, Tokyo
23. ASTM D1037–12 (2017) Standard test method for evaluating properties wood-based fiber and particle panel materials. ASTM International, West Conshohocken, PA
24. GOM Correlate (GOM mbH, Germany), https://www.gom.com/en/products/zeiss-quality-suite/gom-correlate-pro. Accessed 6 June 2023
25. myVGL (VOLUME GRAPHICS, Germany), https://www.volumegraphics.com/en/products/myvgl.html. Accessed 6 June 2023
26. Leijten AJM (2016) The bearing strength capacity perpendicular to grain of Norway spruce—evaluation of three structural timber design models. Constr Build Mater 105:528–535. https://doi.org/10.1016/j.conbuildmat.2015.12.170
27. Tanahashi H, Shimizu H, Suzuki Y (2006) Elastic surface displacements of orthotropic wood due to partial compression based on Pasternak model. J Struct Eng (AIJ) 609:129–136. https://doi.org/10.3130/aijs.71.129_3

28. Kuwamura H (2013) Failure strength of wood in single-bolted joints loaded parallel-to-grain—study on steel-framed timber structures part 16-. J Struct Eng (AIJ) 78(691):1575–1584. https://doi.org/10.3130/aijs.78.1575
29. Noguchi M, Sakata H, Wada A, Miyazawa K (2009) A strength calculation method of single bolted timber joint loaded parallel to the grain. J Struct Eng (AIJ) 74(638):681–690. https://doi.org/10.3130/aijs.74.681
30. Van der Put TACM, Leijten AJM (2000) Evaluation of perpendicular to grain failure of beams caused by concentrated loads of joints. Proceedings of the International Council for Research and Innovation in Building and Construction, CIB-W18 Meeting Thirty-Three, Delft, The Netherlands, paper no. 33–7–7
31. Nakagomi T, Kambe W, Ikura Y (2009) A study with fracture mechanics on evaluation of strength and fracture characteristics for bolted joints with Japanese larch glulam tensile loaded perpendicular to grain. J Struct Eng (AIJ) 74(643):1649–1658. https://doi.org/10.3130/aijs.74.1649
32. Tuhkanen E, Mölder J, Schickhofer G (2018) Influence of number of layers on embedment strength of dowel-type connections for glulam and cross-laminated timber. Eng Struct 176:361–368. https://doi.org/10.1016/j.engstruct.2018.09.005

Publisher's Note